Annual Review of Biomedical Engineering

Frontiers in Cryo Electron Microscopy of Complex Macromolecular Assemblies

Jana Ognjenović,[1] Reinhard Grisshammer,[1]
and Sriram Subramaniam[2]

[1]Laboratory of Cell Biology, Center for Cancer Research, National Cancer Institute, Bethesda, Maryland 20814, USA; email: jana.ognjenovic@nih.gov, reinhard.grisshammer2@nih.gov

[2]University of British Columbia, Vancouver, British Columbia V6T 1Z2, Canada;
email: Sriram.Subramaniam@ubc.ca

Annu. Rev. Biomed. Eng. 2019. 21:395–415

First published as a Review in Advance on
March 20, 2019

The *Annual Review of Biomedical Engineering* is
online at bioeng.annualreviews.org

https://doi.org/10.1146/annurev-bioeng-060418-052453

Keywords

cryo-EM, single-particle analysis, cryo electron tomography,
G protein–coupled receptor, spliceosome, fibril

Abstract

In recent years, cryo electron microscopy (cryo-EM) technology has been transformed with the development of better instrumentation, direct electron detectors, improved methods for specimen preparation, and improved software for data analysis. Analyses using single-particle cryo-EM methods have enabled determination of structures of proteins with sizes smaller than 100 kDa and resolutions of ∼2 Å in some cases. The use of electron tomography combined with subvolume averaging is beginning to allow the visualization of macromolecular complexes in their native environment in unprecedented detail. As a result of these advances, solutions to many intractable challenges in structural and cell biology, such as analysis of highly dynamic soluble and membrane-embedded protein complexes or partially ordered protein aggregates, are now within reach. Recent reports of structural studies of G protein–coupled receptors, spliceosomes, and fibrillar specimens illustrate the progress that has been made using cryo-EM methods, and are the main focus of this review.

Contents

1. INTRODUCTION

The steep increase in the number of Electron Microscopy Data Bank entries over the last decade indicates that cryo electron microscopy (cryo-EM) has found its way into the mainstream of methods used for macromolecular structure determination. Continual advances in every aspect of the pipeline for structure determination using cryo-EM have created significant interest in a wide spectrum of biological disciplines in which the application of these methods could address previously intractable problems. Numerous recent reviews have documented the rise and general application of cryo-EM methods (1–6). In this review, we highlight a selected subset of biological problems that have been particularly challenging to address using existing structural methods, but where the application of cryo-EM is now affording new and unprecedented insights. In Section 2, we provide an overview of some of the critical technical steps involved in the cryo-EM workflow. In Section 3, we highlight three paradigmatic examples (G protein–coupled receptors, spliceosomes, and fibrils) that illustrate what is now possible with cryo-EM in the context of historically challenging problems in structural biology. In Section 4, we briefly outline emerging themes in the use of tomography. Section 5 summarizes.

2. SINGLE-PARTICLE CRYO ELECTRON MICROSCOPY METHODOLOGY

Cryo-EM has evolved into a powerful structural biology method for visualizing a wide range of biological specimens in a near-native state (5, 7–13). Initially, the major advances in the field came from studies of highly symmetrical viral particles and large, stable, multicomponent complexes such as ribosomes (14–17). More recently, barriers such as practical resolution limits (18, 19), size of macromolecular targets (20–22), lack of internal symmetry (23), and sample solubility (24–31) have in many cases been overcome. Although many critical improvements have propelled the application of cryo-EM methods, progress in all aspects of the workflow, ranging from specimen preparation to better detectors and improved image processing, can be expected in the near future (6, 32–34).

2.1. Key to Success: Sample Preparation

The likelihood of successful structure determination depends directly on sample quality, and thus sample preparation. In a broad sense, protocols for sample preparation for cryo-EM methods resemble those for X-ray crystallography and NMR. However, there are both challenges and advantages that are unique to cryo-EM, as reviewed below.

One of the most advantageous features of single-particle cryo-EM over X-ray crystallography is the requirement for only small quantities of pure sample instead of well-diffracting crystals. This can be transformative for a number of macromolecular targets that are difficult to obtain in large quantities for crystallization trials and/or are recalcitrant to crystallization (5). There are important differences in the nature of the sample requirements. Crystallization is essentially a purification technique that captures a particular sample in a specific, low-energy state within an ensemble of conformations. However, the same protein solution that results in diffracting crystals may adopt multiple conformational states in solution. This problem is accentuated for multicomponent macromolecular complexes, where weak association may lead to dissociation of components from a given assembly. The degree of difficulty in structure determination is directly related to the conformational homogeneity of the specimen, although powerful image processing methods are available to classify and resolve discrete conformations that are present in mixtures (35). These methods are especially useful for following time-resolved changes in conformation, when specimens are plunge-frozen at different points in time after the start of a reaction sequence (36).

Classical biochemical and biophysical tools can be useful in addressing some of the challenges posed by sample heterogeneity. Optimization of the buffer composition may stabilize the target sample while minimizing the impact of compounds that contribute to unwanted electron scattering and decrease the signal-to-noise ratio (SNR) (37). Dynamic light scattering and differential scanning fluorimetry devices provide information about sample polydispersity, size distribution, and ultimately sample stability (38). Labile multisubunit macromolecular complexes may require mild cross-linking for structural stabilization using different cross-linking agents [e.g., glutaraldehyde, *bis*(sulfosuccinimidyl) suberate, *bis*(sulfosuccinimidyl) glutarate] in conjunction with the gradient-based cross-linking method GraFix, where the sample is subjected to ultracentrifugation separation through simultaneous density and cross-linker gradients (39).

Membrane proteins are notoriously recalcitrant to crystallization and structure determination by X-ray crystallography, but cryo-EM offers an alternative and perhaps superior route to high-resolution structure determination (see Reference 40 for a recent review). **Table 1** illustrates the variety of membrane protein targets whose structures were reported in 2018 at a reported resolution of 4 Å or less. Since purification of integral membrane proteins necessitates their extraction from the native membrane environment by detergents, the presence of the detergent may introduce artifacts that pose challenges for structure determination (40, 41). For example, detergent monomers alter the surface tension of the sample, which could lead to a thicker ice layer during grid preparation. Free micelles in the sample may decrease the SNR and could be mistakenly identified as protein particles in the selection of projection images for three-dimensional (3D) reconstruction (i.e., the particle picking step). Also, detergent bound to the membrane protein cores can form belts of inconsistent sizes, causing problems during data processing (40). A case study on detergent background in negative-stain electron microscopy concluded that decyl-maltoside and digitonin were acceptable for structural studies; although reduced, the background was still noticeable below the critical micellar concentration (41). GraDeR, a method that involves gradual removal of the excess of detergent micelles, uses concurrent density gradient and size separation (42). The reader is referred to **Table 1** for a list of the detergents used for the purification of various membrane protein targets.

Table 1 Selected membrane protein structures by single-particle analysis with a reported resolution ≤4 Å as of 2018[a]

Membrane protein	Resolution (Å)	EMD code of cryo-EM maps	Comments[b]	Reference
Ion channels				
Insect Na$_V$PaS bound with TTX and Dc1a	2.6, 2.8, 3.2	6995, 6996, 6997	Digitonin, Cu grid	126
Nematostella TRPM2 cation channel	3.1	7542	Digitonin, Au grid	127
Human TRPM4 cation channel	3.7	7299	Digitonin, Cu grid	128
Mouse TRPM7 cation channel	3.7, 4.1	7297, 7298	Amphipol (PMAL–C8), Cu grid	24
Insect odorant-gated ion channel Orco	3.5		Digitonin, Au grid	129
Mouse two-pore channel (TCP1)	3.2, 3.4	7434, 7435	GDN, Au grid	130
Fungal and zebrafish mitochondrial calcium uniporter	3.2, 8.5	7971, 7972	Digitonin/cardiolipin, Au grid	131
Neurospora mitochondrial calcium uniporter	3.7	8911	BS3 cross-link, amphipol, nanodisc, Au grid	31
Fungal mitochondrial calcium uniporter	3.8, 5.0	7826, 7828	Nanodisc (saposin), Au grid, VPP	132
Human lipid-gated cation channel TRPC3	3.3	7620	Digitonin, Au grid	133
Mouse nonselective cation channel TRPC4	3.3	6901	Digitonin, Cu grid	134
Zebrafish nonselective cation channel TRPC4	3.6	4339	Amphipol, Cu grid	135
Human inositol trisphosphate receptor	3.3–6.0	7978–7996	Digitonin, Cu grid	136
Spirochaeta SthK cyclic nucleotide–gated potassium channel	3.4, 3.5	7482, 7483, 7484	Nanodisc, Au grid, fluo-FC8	30
Human CLC-1 chloride ion channel	3.4, 3.4	7544, 7545	DDM, Au, Cu grid	137
Human SK4/calmodulin channel complex	3.4, 3.5, 4.7	7537, 7538, 7539	DDM, Au grid	138
Mouse volume-regulated anion channel LRRC8	3.7, 4.2, 5.0, 8.0	4361, 4362, 4366, 4367	Digitonin, Au grid	139
Chicken acid sensing ion channel	3.7	7009	DDM/CHS, Au grid	140
Human polycystin 2-l1 ion channel	3.1	8912	Amphipol (PMAL–C8), Cu grid	26
Electron transport, oxidative phosphorylation				
Blastochloris reaction center light-harvesting complex 1	2.9	3951	DDM, Cu grid	141
Maize photosystem I supercomplex with light-harvesting complexes I and II	3.3	6932	DDM/digitonin, sucrose density gradient, Cu grid	142
Red algae photosystem I with light-harvesting supercomplex	3.6, 3.6	6929, 6930	DDM, sucrose density gradient, Cu grid	143
Chloroplast F$_1$F$_o$ ATP synthase	3.1, 3.6, 4.2, 4.3	4270, 4271, 4272, 4273	Nanodisc	25
Yeast vacuolar ATPase V$_o$	3.5	7348	Nanodisc, Au grid	144
Yeast mitochondrial ATP synthase (F$_1$F$_o$)	3.8, 4.2, 3.6, 4.1	7546, 7547, 7548, 7549	Nanodisc, Cu grid	145
Mouse mitochondrial complex I	3.3, 3.9	4345, 4356	DDM, PEGylated Au grid	146
Pyrococcus membrane-bound hydrogenase	3.7	7468	DDM, Cu grid	147
Flavobacterium alternative complex III in supercomplex with cytochrome oxidase	3.4, 3.6, 3.6	7286, 7447, 7448	SMALP (no detergent), Au grid	148

(*Continued*)

Table 1 (*Continued*)

Membrane protein	Resolution (Å)	EMD code of cryo-EM maps	Comments[b]	Reference
Multidrug transporters				
Human ABCG2	3.1, 3.6	3953, 4246, 4256	Nanodisc, Cu grid	27
Human P-glycoprotein	3.4	7325	DDM/CHS, Au grid, fluo-FC8	149
Chimeric human–mouse ABCB1	3.6, 4.1, 4.5, 4.6, 6.2	4281, 4282, 4283, 4284, 4285	Disulfide-trapped; LMNG/CHS, amphipol, lacey carbon grid	150
Pentameric Cys-loop receptors				
Rat $GABA_A$ receptor	3.1, 3.8	8923, 8922	DDM, Au grid, graphene oxide	151
Human nicotinic receptor	3.7, 3.9	7535, 7536	DDM/CHS, Au	152
Transporter				
Human neutral amino acid transporter ASCT2	3.9	4386	DDM/CHS, Au grid	153
Others				
Yeast oligosaccharyltransferase	3.3, 3.4	4161, 4257	Nanodisc, Cu grid	154
Human patched–sonic hedgehog	3.5, 3.8	7795, 7796	Amphipol, Au grid	29
Human patched–sonic hedgehog	3.9, 4.1, 3.6	7963, 7964, 7968	Digitonin, Cu grid	155
Mouse gasdermin A3 membrane pore	3.8, 4.2, 4.6	7449, 7450, 7451	Cholate, C12E8, Cu grid, $HgCl_2$-treated	156

[a] GPCR entries are listed in **Table 2**.

[b] This column contains information about the use of detergent, amphipol, nanodisc, cross-linking, grid type, additive for grid preparation, and phase plate.

Abbreviations: ASCT, alanine, serine, cysteine transport; C12E8, octaethylene glycol monododecyl ether; CHS, cholesteryl-hemisuccinate; cryo-EM, cryo electron microscopy; DDM, dodecyl-maltoside; EMD, Electron Microscopy Data Bank; fluo-FC8, fluorinated Fos-choline-8; GABA, γ-aminobutyric acid; GDN, glyco-diosgenin; GPCR, G protein–coupled receptor; LMNG, lauryl maltose neopentyl glycol; PEG, poly(ethylene glycol); PMAL, poly(maleic anhydride-*alt*-1-decene) substituted with 3-(dimethylamino) propylamine; SMALP, styrene maleic acid copolymer–lipid particle; TRPC, transient receptor potential cation; TRPM, transient receptor potential cation channel subfamily M; TTX, tetrodotoxin; VPP, Volta Phase Plate.

An alternative approach is the preparation of detergent-free membrane protein samples. This approach includes the use of amphiphilic polymers or amphipols that bind to membrane proteins with stronger affinity than detergents (43) and nanodiscs that mimic the native membrane bilayer (**Table 1**) (44, 45). A recent study used peptidiscs, composed of short, amphipathic, bihelical peptides (46), and engineered nanostructured β-sheet peptides, which form filaments in solution but undergo reconstruction once the membrane protein is added (47). Styrene maleic acid copolymer–lipid particles (SMALPs) are also beneficial to membrane protein studies (48) and have been successfully used for structure determination of proteins such as the *Escherichia coli* multidrug efflux transporter AcrB (28).

2.2. The Air–Water Interface: Grid Preparation

A central element of the cryo-EM pipeline is the process of vitrification, in which a bulk suspension of the solution of interest is first reduced to a thin film by blotting, followed by rapid plunge-freezing into a liquid cryogen such as ethane cooled by liquid nitrogen (49). Currently, vitrification of EM samples is partially automated in commercially available plunge-freezing stations that offer options for humidity and temperature control (50). The length of time between blotting and freezing can be shortened to be within ∼100 ms, but protein denaturation at the air–water interface remains a major impediment to sample integrity. This is because proteins diffuse from the bulk of an aqueous solution to the air–water interface within milliseconds (51), giving rise to multiple opportunities for the protein to be subject to denaturing forces during specimen preparation.

Numerous attempts have been made to optimize grid preparation so that the interaction between particles and buffer surfaces is altered. The most common modifications include changes in the buffer composition (e.g., pH, additives, detergents, ligands), the use of grids with a support film [e.g., thin carbon layer (52), graphene oxide], or the use of grids with affinity support films (e.g., streptavidin monolayer, nickel–nitrilotriacetic acid, antibody-functionalized film) (5). D'Imprima et al. (51) performed a quantitative analysis of protein denaturation at the air–water interface, comparing unsupported grids and grids coated with a layer of graphene rendered hydrophilic with 1-pyrene-carboxylic acid (53). Only a minority of the fatty acid synthase particles used in their study retained integrity in unsupported vitreous films. However, use of EM grids with hydrophilized graphene resulted in a strong tendency of fatty acid synthase to locate at the graphene–water interface, preserving the integrity of the complex (51). Efforts to discourage preferential particle orientation (and improve the ice thickness distribution of the grid) include saturation of the drop surface with, for example, fluorinated detergents (**Table 1**) (44, 54, 55).

Most recent approaches include the grid-making methods devoid of the blotting step. One of these methods is the blotless Spotiton method, which uses a piezoelectric inkjet dispenser depositing picoliters of sample onto special nanowire self-blotting grids. The method is optimized to wick away the excess of the liquid as soon as the sample touches the nanowires, leaving only a thin layer of the sample on the grid (56). Glaeser et al. (57) are developing another interesting approach in which, instead of blotting, sample thinning is accomplished by creating the surface tension gradient using a flow of a volatile surfactant under conditions of high humidity.

2.3. Engineering Advances and Programming Enthusiasts: Hardware and Software

Innovations in the design of electron microscopes and related accessories have continued to advance over the last decade. These have included tools for robotic handling of specimens with an autoloader; lens design that permits stable operation over a wide range of voltages; energy filters for imaging of thicker specimens; phase plates for enhanced contrast (58); and most importantly, the switch from the use of photographic film and charge-coupled devices to direct electron detectors, which has resulted in dramatic improvements in image quality and the ability to compensate for beam-induced specimen movement during electron-beam exposure (59). The use of these detectors in conjunction with automated data-collection procedures implemented in many software packages [e.g., SerialEM (60), Latitude (GATAN Inc.), Leginon (61), EPU (Thermo Fisher)] has enabled cryo-EM data collection to become much more streamlined and user friendly. A variety of software packages are available to analyze the data (2, 62–64), empowering expert and nonexpert users alike to convert the collected data into useful 3D structures. The democratization process is being further accelerated with the growth of regional and national cryo-EM facilities, which provide users access to state-of-the-art instrumentation and, in some cases, access to on-the-fly preprocessing routines that incorporate both motion correction and contrast transfer function estimation while data are being collected (65).

3. FRONTIER APPLICATIONS

3.1. G Protein–Coupled Receptor–G Protein Complexes

G protein–coupled receptors (GPCRs) mediate many responses of cells to external stimuli. Upon activation by a ligand, the receptor interacts with heterotrimeric G proteins and/or arrestins, initiating downstream signaling (66). Insights into the allosteric coupling between ligand binding and G protein or arrestin interaction are arising from a limited number of GPCR structures in inactive and active conformations, as well as from spectroscopic and computational analyses. However, understanding of the high-resolution structural changes during GPCR activation, signaling, and regulation is necessary to conceptualize the complex pharmacology of GPCRs.

GPCR–heterotrimeric G protein complexes have been exceedingly difficult targets for 3D crystallization and structure determination by X-ray crystallography owing to the intrinsic conformational flexibility and instability of the complex. The first active-state crystal structure of a GPCR, solved in 2008, was that of opsin complexed with GαCT, a synthetic peptide derived from the C terminus of the transducin α subunit (67). This was followed in 2011 by the structure of the β_2-adrenergic receptor in complex with the heterotrimeric G protein Gs, composed of Gαs, β_1, and γ_2 subunits (68), reflecting a heroic effort in methods development. The stability of the receptor complex was enhanced by use of the then newly available highly stabilizing lauryl maltose neopentyl glycol (LMNG) detergent (69). A modified lipid for lipidic cubic-phase crystallization (68, 70) was designed to accommodate the large hydrophilic components of the β_2-adrenergic receptor–Gs assembly. Lastly, use of a nanobody (Nb35) prevented dissociation of the complex and further facilitated crystallogenesis (68). In 2016, the third crystal structure, that of the adenosine A_{2a} receptor in complex with an engineered minimal G protein (mini-Gs) composed of a single domain from the Gαs subunit, was published (71), signifying years of determination to engineer a minimal G protein to facilitate crystallization of GPCRs in their active conformation (72). Despite the availability of an array of tools, X-ray structure determination of GPCR–G protein complexes remains intractable, as the growth of well-ordered, 3D crystals continues to present a major obstacle for many membrane protein targets.

Single-particle cryo-EM does not require the formation of crystals for structure determination. Despite the challenges in biochemistry resulting from the intrinsic conformational heterogeneity, there is a growing list of GPCRs (**Table 2**) whose structures have now been analyzed using cryo-EM, starting with the 150-kDa complex of the calcitonin receptor bound to heterotrimeric Gs (73). As of late 2018, eight additional cryo-EM structures of GPCR–G protein complexes have been reported—the glucagon-like peptide 1 receptor–Gs complex (74, 75), the adenosine A_{2a} receptor coupled to an engineered heterotrimeric G protein (76), the μ opioid receptor bound to Gi (77), the adenosine A_1 receptor–Gi complex (78), the rhodopsin–Gi complex (79), and the serotonin 5HT1B receptor coupled to Go (80)—all in an astonishing span of only 2 years. Most recently, the structure of the human calcitonin gene–related peptide (CGRP) receptor, a heterodimer of calcitonin receptor–like receptor and receptor activity–modifying protein 1 in complex with Gs, has been published (81).

As discussed in Section 2.2, successful structure determination by cryo-EM requires specimen preparation procedures that can withstand potential denaturation from the interfacial forces at the air–water interface during grid preparation. Furthermore, inherent flexibility between the complex components must be minimized to obtain stable 3D classes with detailed features for all subunits. The GPCR–G protein complexes analyzed by cryo-EM to date were prepared under highly stabilizing buffer conditions, using the LMNG detergent or digitonin, with the inclusion of lipid in some cases (**Table 2**). As a result, the complexes were robust enough to yield good-quality data. Even so, in all cases to date, only a small fraction of the molecular projection images was utilized to obtain the final density map, potentially because a significant proportion of the protein complexes were denatured at the air–water interface (74–80).

The Volta Phase Plate (VPP) (58) has been used in approximately half of the reported GPCR structures (73, 74, 76, 78, 80, 81), and a comparison of the structure with and without use of

Table 2 GPCR–G protein structures determined by single-particle cryo-EM

GPCR–G protein complex	Nominal global resolution (Å)	EMD code of cryo-EM maps	Comments	Antibody fragment	Reference
Class A GPCRs					
Human A_{2a} receptor–Gs	4.1	4390	LMNG, Au grid, ±VPP	Nb35	76
Mouse μ opioid receptor–Gi	3.5	7868, 7869	LMNG/GDN/CHS, Cu grid	scFv16	77
Human A_1 receptor–Gi2	3.6	7835	LMNG/CHS, Cu grid, VPP	None	78
Human rhodopsin–Gi	4.5	7517	Digitonin, Au grid	Fab_50	79
Human serotonin 5HT1B receptor–Go	3.8	4358	Au grid, VPP	None	80
Class B GPCRs					
Human CGRP receptor (heterodimer of calcitonin receptor–like receptor and receptor activity–modifying protein 1)–Gs	3.3	8978	LMNG/CHS, Cu grid, VPP	Nb35	81
Human calcitonin receptor–Gs	4.1	8623	LMNG/CHS, Cu grid, VPP	Nb35	73
Human GLP1 receptor–Gs	3.3	7039	LMNG/CHS, Cu grid, VPP	Nb35	74
Rabbit GLP1 receptor–Gs	4.1	8653	LMNG, cholesterol, POPG, GDN, Cu grid	Nb35	75

Abbreviations: CGRP, calcitonin gene–related peptide; CHS, cholesteryl-hemisuccinate; cryo-EM, cryo electron microscopy; EMD, Electron Microscopy Data Bank; GDN, glyco-diosgenin; GLP1, glucagon-like peptide 1; GPCR, G protein–coupled receptor; LMNG, lauryl maltose neopentyl glycol; POPG, 1-palmitoyl-2-oleoyl-*sn*-glycero-3-phosphoglycerol; scFv, single-chain variable fragment; VPP, Volta Phase Plate.

the phase plate has been reported for the A_{2a} receptor–Gs complex (76). While the presence of the VPP resulted in better resolution in combination with a given detector, the improvement was found to be sample dependent, and more comparisons will be required to understand the variability in resolution between samples (76).

All receptor–G protein complexes, except A_1 receptor–Gi (78) and 5HT1B receptor–Go (80), were prepared in the presence of antibody fragments. For complexes with the Gs-coupled receptors for calcitonin (73), CGRP (81), glucagon-like peptide 1 (74, 75), and 5′-*N*-ethylcarboxamidoadenosine (A_{2a} receptor) (76), the nanobody Nb35 was utilized; Nb35 binds at the Gαs–Gβ interface, stabilizing the respective GPCR complex in detergent solution. Nb35 was first used in the crystal structure determination of the β_2-adrenergic receptor with Gs (68). The μ opioid receptor–Gi complex (77) was stabilized by a single-chain variable fragment (scFv16) that binds to heterotrimeric Gi. In contrast to Nb35, scFv16 binds an epitope containing the αN helix of Gαi and the β propeller of Gβ, more than 20 Å away from the receptor–Gi interface. Subtraction of the scFv16 signal from raw particle images improved the map to an overall global resolution of 3.5 Å (77). The rhodopsin–Gi complex was prepared in the presence of Fab_50, binding far from the rhodopsin–Gi interface (**Figure 1**) (79). The map at a nominal global resolution of 4.5 Å showed well-defined density for the rhodopsin seven-transmembrane domain, the Gαi Ras-like domain, and the Gβ and Gγ subunits. The position of the α-helical domain (AHD) of

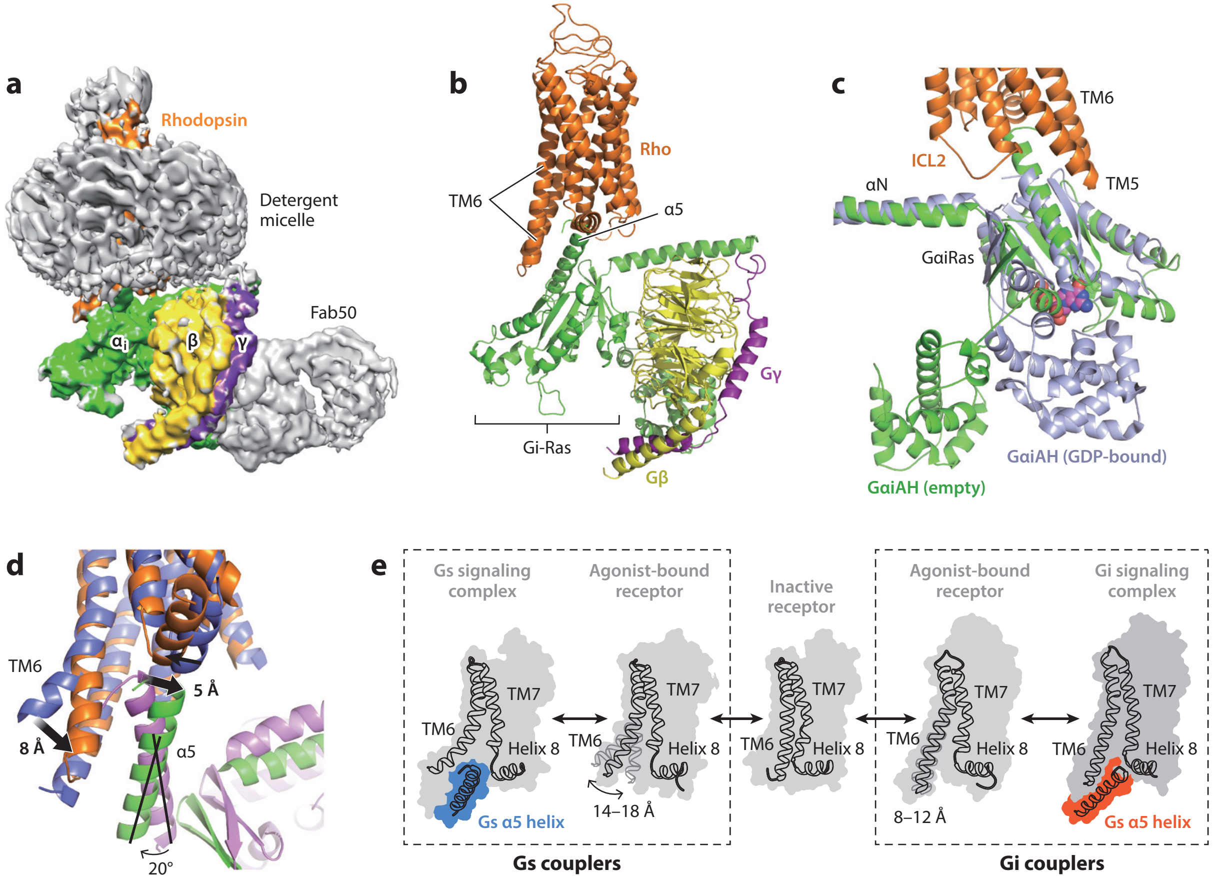

Figure 1

Structural differences in GPCR–G protein complexes. GPCRs activate cellular signaling by binding to G proteins and arrestins (not shown). Stimulatory G proteins are called Gs, whereas inhibitory G proteins are called Gi/o. G proteins consist of three subunits: Gα, Gβ, and Gγ. Part of the interface between the receptor and the G protein is formed by the C-terminal residues of the Gα subunit, termed the α5 helix. Many GPCRs bind selectively to Gs or Gi/o, but the basis of this selectivity was unclear until recently. The figure compares rho–Gi (79) with β_2AR–Gs (68). (*a*) Cryo-EM map of the rho–Gi–Fab complex at a nominal global resolution of 4.5 Å. (*b*) Ribbon diagram representation of the rho–Gi structure. (*c*) Comparison of the nucleotide-free (empty) rho–Gi complex with inactive GDP-bound Gi (Protein Data Bank code 1GG2). Binding of Gi to rhodopsin results in conformational changes within the Gαi Ras domain, weakening GDP binding. The release of GDP from Gαi results in a marked displacement of the AHD from the Gαi Ras domain. The mechanism of rho-mediated Gi activation is similar to that of β_2AR-mediated Gs activation, suggesting a common mechanism of GPCR-mediated G protein activation. (*d*) Structural differences between TM6 (rho in orange, β_2AR in blue) and the α5 helix (Gαi in green, Gαs in purple). (*e*) Schematic of conformational states of Gs- and Gi/o-coupled receptors. The cartoon shows the schematic positions of the TM6 and TM7 of the receptors, and the α5 helix of the Gα subunit of GPCRs in complex with Gs and Gi/o. The outward displacement of TM6 is smaller in Gi/o than in Gs complexes, and the Gi/o α5 helices are rotated and slightly moved toward TM7, away from TM6. Abbreviations: AHD, α-helical domain; cryo-EM, cryo electron microscopy; GPCR, G protein–coupled receptor; rho, rhodopsin; TM, transmembrane; β_2AR, β_2-adrenergic receptor. Figure adapted from Reference 79.

Gαi was well defined owing to the direct stabilization of this domain by the Fab fragment, which also interacted with Gβγ (79).

Gs-bound receptor structures provided insight into the general activation mechanism of Gα proteins. Binding of an activated receptor induces displacement of the α5 helix and conformational changes within the Ras domain of the G protein. The rearrangement of the loop between β6 and the $\alpha5$ helix of Gα, away from the nucleotide binding pocket, and changes in the $\beta1$–$\alpha5$ loop (P-loop) weaken GDP binding. Because GDP helps stabilize the closed-domain conformation of Gα, the release of GDP from Gα allows a marked displacement of the AHD from the Gα Ras domain. The comparison between the Gs-coupled and Gi/o-coupled receptor structures showed how GPCRs selectively activate a particular family of G proteins (**Figure 1**). For example, there are no interactions between the receptors and the Gβ subunits in the Gi/o-bound receptor structures. Furthermore, the positioning of the Gi/o $\alpha5$ helices differs from that of the respective helices in the GPCR–Gs complexes, and transmembrane domain TM6 is displaced outward from the receptor core to a lesser extent than in the Gs-occupied receptors. The smaller displacement of TM6 in Gi-coupled GPCRs may preclude binding of Gs, possibly explaining how GPCRs can bind selectively to Gi/o proteins.

To date, observations in GPCR–G protein complexes have shown that sample quality and especially stability determine success or failure of the structure determination, not only in X-ray crystallography but also (perhaps more so) in cryo-EM. Thus, the development of approaches, applicable to all GPCRs, for stabilization of the highly dynamic complexes will be essential to understanding the plethora of ligand-specific signaling responses.

3.2. Spliceosome

Another prominent example of single-particle cryo-EM comes from structural studies of the precursor messenger RNA (mRNA) splicing machinery: the spliceosome. For more than 30 years, the catalytic mechanism and intricate structural choreography of the spliceosome have been under intense scrutiny (82). The problem of mRNA splicing captivates scientists not only because of its fundamental aspects but also because unlocking its mysteries offers a plethora of opportunities for rational interventions in pathological conditions. Multiple efforts have resulted in structural resolution by X-ray crystallography, which, albeit significant, represents snapshots of only relatively small, individual components (83, 84). It is now clear that the sheer complexity of the machinery could not have been, and perhaps cannot be, captured by crystallographic approaches. This is due to both the large size and complexity of the target.

Although the size of the spliceosome is comparable to that of the ribosome, there are clear distinctions between these two supramolecular particles that explain why the latter could have been initially studied in great detail with X-ray crystallography and why a similar approach was inapplicable for the former. The ribosome represents a stable cellular machine in which well-defined RNA scaffolds, organized into two subunits, are arrayed with proteins that play an important role but do not participate directly in catalytic events. Also, aside from conformational movements of stalk segments and subunit rotational movements during protein synthesis, ribosomal RNA (rRNA) is a relatively stable structure (85). In contrast, the spliceosome is a highly dynamic multimegadalton ribonucleoprotein particle that undergoes changes in both stoichiometry and composition during mRNA splicing. Spliceosome proteins are critical not only for the structure of specific spliceosome intermediates but also for actively engaging in the splicing process, in contrast to ribosomal proteins (86). Moreover, spliceosomal RNA is not as ordered as rRNA; it is rather flexible. In fact, it is this flexibility that enables successful mRNA splicing because only in the presence of such an RNA can various intermediates along the catalytic cycle be attained. The inherent transient nature of the spliceosome was the major hurdle for classical X-ray crystallographic studies that relied on large quantities of a well-defined, homogeneous sample. However, in recent years several cryo-EM studies have been completed on the yeast spliceosome, and these have unearthed a wealth of information.

The yeast spliceosome is composed of five ribonucleoprotein complexes [i.e., the U1, U2, U4, U5, and U6 small nuclear ribonucleoproteins (snRNPs)] and a variety of proteins that are able to recognize and assemble around specific intron sequences of precursor mRNA (86). A series of highly organized and regulated steps (**Figure 2**) starts with the recognition of a 5′ splice site and a branching point by U1 and U2 snRNPs. This is followed by binding of preformed triple U4/U6.U5 snRNPs, which form precatalytic complex B. Activation of complex B (B*) occurs with a significant rearrangement of constituents; U1 and U4 snRNPs dissociate concurrently with the recruitment of NTC (nineteen protein complex) and NTR (nineteen-related complex). The product of the step I reaction is a phosphodiester bond between the branch point adenosine 2′-OH and the 5′ splice site (complex C). Further steps involve additional rearrangements of the spliceosome to align exons (complex C*) for the step II reaction. The final product, spliced mRNA, is released, and intron lariat spliceosome (ILS) is dissembled and reused for the next splicing cycle (87).

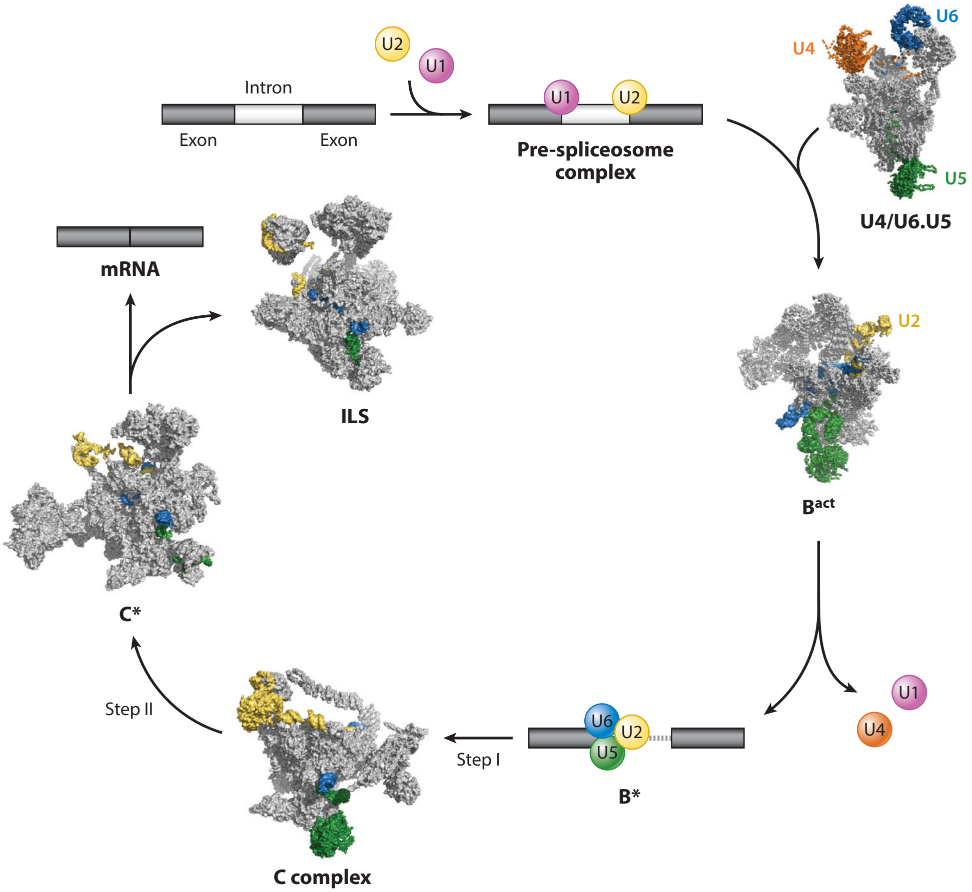

Figure 2

Spliceosome reaction cycle. U1 and U2 snRNPs bind to the branching point at the exon–intron boundary and the 5′ end of the downstream exon of the mRNA, respectively. Upon binding of U4/U6.U5 (PDB code 3JCR; EMD-6581) (121), the preactivated complex (B^{act}; PDB code 5LQW; EMD-4099) (122) is established. The dissociation of U1 and U4 yields active B* complex. Successive step I and II reactions yield C (PDB code 5GMK; EMD-9525) (123) and C* complexes (PDB code 5XJC; EMD-6721) (124), respectively. The final reaction products are the ILS complex (PDB code 3JB9; EMD-6413) (125) and spliced mRNA. Abbreviations: EMD, Electron Microscopy Data Bank; ILS, intron lariat spliceosome; mRNA, messenger RNA; PDB, Protein Data Bank; snRNPs, small nuclear ribonucleoproteins.

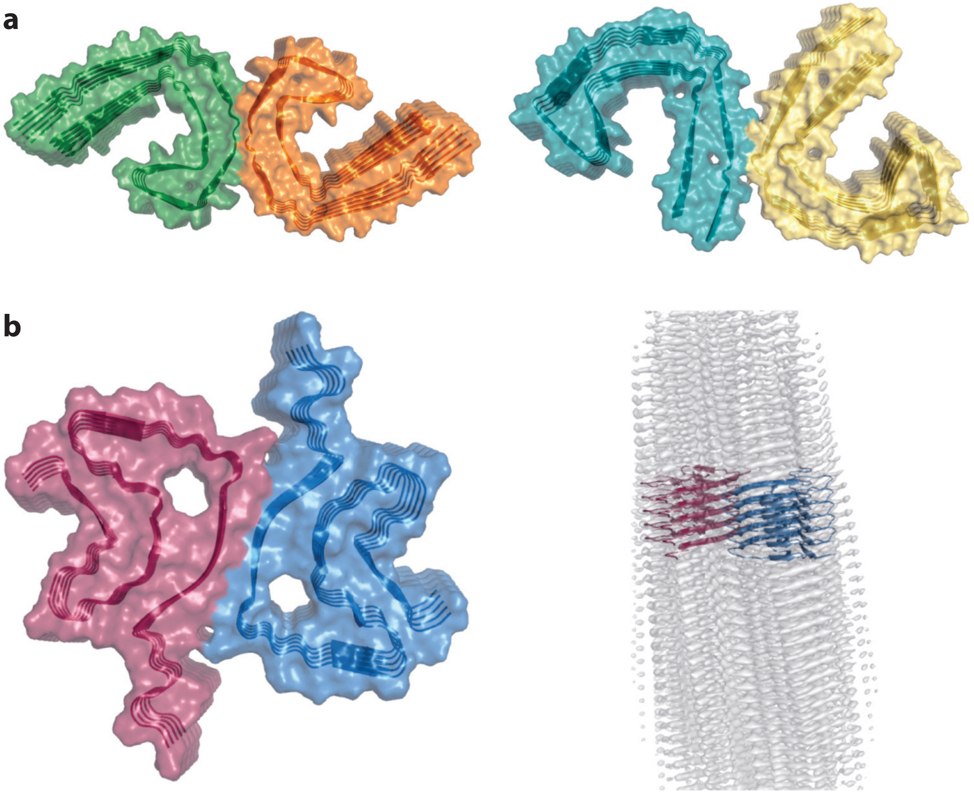

Figure 3

Cryo-EM structures of fibrils. (*a*) The presence of tau filaments in a patient's brain is characteristic of Alzheimer disease. Ribbon diagrams of structures of (*left*) paired-helical (PDB code 5O3L) and (*right*) straight tau filaments (PDB code 5O3T) (99). (*b*) (*left*) A ribbon diagram of the structure of the α-synuclein fibril dimer (PDB code 6H6B) and (*right*) a cryo-EM map of a larger fibril segment (EMD-0148) typical for patients with Parkinson's disease (101). Abbreviations: cryo-EM, cryo electron microscopy; EMD, Electron Microscopy Data Bank; PDB, Protein Data Bank.

Visualization of this process was enabled by cryo-EM methods. Starting with the purified yeast spliceosome, Yan et al. (88) utilized computational advances in cryo-EM to perform in silico purification. This approach revealed structures of three different spliceosome stages: precatalytic complex B, complex C*, and ILS. In addition to the yeast spliceosome, significant efforts have been made to illuminate the analogous process in humans, with sample preparation aided by the use of mild chemically induced protein cross-linking (89–91).

3.3. Fibrils

Another group of macromolecules that attract significant scientific interest consists of proteins that form fibrils (**Figure 3**). These particular proteins are considered the principal causative agents in many neurodegenerative diseases but are poorly understood at the structural and functional levels (92–94).

It is thought that proteins synthesized in a cell typically adopt the most thermodynamically stable conformation. Native proteins can, however, undergo an abnormal conformational transition, wherein α helices are converted to β sheets or to partially ordered states. Misfolded, and presumably toxic, proteins serve as a substrate for rapid nucleated growth of linear aggregates or amyloid fibrils (95). These fibrils are insoluble and resistant to degradation, proteolysis, and biological clearance. Amyloid deposits of serum amyloid A, light-chain immunoglobulin G, and transthyretin have been strongly implicated in pathologies of various organ systems (reviewed in Reference 96). In addition, it is thought that accumulation of fibrils of β-amyloid, α-synuclein, tau, and prion protein peptide either directly causes neuronal death or is a manifestation of a pathological condition. Thus, a better understanding of fibril structure and the mechanisms of fibril formation may provide new avenues for therapies that target both the development and progression of neurodegeneration of the human brain.

Structural studies of fibrils have been hindered because of their variable nature. Although fibrils exhibit locally ordered stacks of protofilaments, minor changes such as twists, bends, and/or axial flexibilities can result in different fibril morphology at the global level (97). These structural departures hamper the ability to obtain pure sample, and even if one is obtained, it is almost certain that only a fraction of the entire fibril will be visualized. Moreover, most recent findings and observations suggest that fibrils exhibit significant structural polymorphisms both in vitro and in patient- and animal-derived samples. The intrasample polymorphism is not obviously dependent on amino acid sequence or other features, which brings the complexity of fibril studies to another level. Different polymorphs may cause different aggregation kinetics, oligomerization dynamics, and disease phenotypes, which may presumably complicate the development of therapies. Recently, mathematical analyses have been employed to better understand and perhaps predict fibril polymorphisms (98).

Because of improvements in sample preparation and structural methods, a number of different fibril structures have recently been determined using cryo-EM helical image processing. A cryo-EM study of patient-derived tau fibrils, the major hallmark of tauopathies (Alzheimer disease in this case), revealed structural differences in the core of ultrastructural polymorphs, paired-helical and straight tau fibrils, derived from two identical protofilaments (99). This finding indicates that different tau fibril conformers might be connected to different, specific neuropathies within the sample derived from the brain tissue of the same patient. Similar cryo-EM studies were done on a patient-derived sample from an individual afflicted with Pick's disease (100). In this case, additional tau fibrils, narrow and wide Pick's fibrils, were described at near-atomic resolution. The narrow tau fibrils are composed of one protofilament and are conspicuously different from tau fibrils found in Alzheimer disease. Another fibril structure comes from a study completed on almost-full-length α-synuclein fibrils, which are linked to Parkinson disease. Given the observed protofilament interactions, the authors of that study proposed an underlying mechanism for α-synuclein fibril elongation (101).

It is not clear whether the presence and formation of fibril structures are the cause or the product of neurodegenerative diseases. However, it is clear that cryo-EM methods could dramatically improve our understanding of these mysterious structures and perhaps facilitate the development of novel therapies.

4. CRYO ELECTRON TOMOGRAPHY AND SUBTOMOGRAM AVERAGING

Electron tomography at cryogenic temperatures (cryo-ET) is an approach to structure determination of biological entities such as whole cells and viruses that are unique and do not lend themselves to averaging using single-particle cryo-EM methods. An important use of tomography is in combination with subvolume averaging, which allows for 3D averaging of relative homogeneous components within viruses and cells, providing a powerful opportunity to study proteins in their native physiological environment (3, 102–104). Thus, cryo-ET provides a route to macromolecular structures without the need to first express and purify the components (4). This section provides only a brief overview of cryo-ET and subtomogram averaging; we refer the reader to recent reviews and references therein for more details (3, 4, 103, 105).

Methods for imaging of whole viruses and cells typically use the same protocol for plunge-freezing as for single-particle specimens, although the resulting specimens tend to be considerably thicker because the larger dimensions of the viruses or cells dictate this thickness. Thinning the samples with focused ion beams both offers a way to control the specimen thickness and presents a new approach to the examination of structural aspects of the cell interior, such as the nucleus (4, 106, 107).

Methods of tomographic data collection involve rotation of the vitrified specimen to a limited angular range (typically ±70°), and the resulting projection images are combined computationally to obtain a tomogram of the region of interest. A variety of schemes are used to obtain this series of tilted images, ranging from a continuous progression from negative to positive tilts to dose-symmetric tilt series, where data collection starts at zero and progresses to increasingly high negative and positive tilt angles (108–110).

Through the use of specialized tilt schemes and methods, the high-resolution structure of the human immunodeficiency virus 1 (HIV-1) CA–SP1 (capsid–spacer peptide 1) has recently been reported (109, 111). Immature HIV-1 buds from the plasma membrane before proteolytic cleavage of the viral Gag polyprotein induces maturation, which can be blocked by maturation inhibitors, abolishing virus infectivity. This study used plunge-frozen immature virus–like particles, assembled in vitro from the purified CA and SP1 region of the Gag polyprotein, in the presence (3.9-Å resolution) or absence (4.5-Å resolution) of maturation inhibitors; as well as an immature, protease-defective HIV-1 particle (4.2-Å resolution). An atomic model, based on the 3.9-Å-resolution map, provided the template to catalog mutations, deletions, and polymorphisms that confer resistance to maturation inhibitors, showing that the sites of mutations do not coincide with potential drug-binding pockets. This finding implies that maturation inhibitors do not sterically block the proteolysis site, but rather stabilize the immature Gag protein. As proteolytic cleavage requires unfolding of Gag, HIV-1 seems to develop maturation inhibitor resistance by destabilizing its immature form (109). A concurrent X-ray crystallographic study reached similar conclusions (112).

Subnanometer resolution structures have been reported for other viral and bacterial objects. Bharat et al. (108) examined the S-layer of the gram-negative bacterium *Caulobacter crescentus* by cryo-ET and subtomogram averaging of cell stalks, and compared the resulting 7.4-Å structure with the X-ray structure of the purified S-layer protein RsaA. Wan et al. (110) reported the structure of the Ebola virus nucleocapsid within intact viruses and recombinant nucleocapsid-like assemblies, revealing the identity and arrangement of the nucleocapsid components. This study allowed the authors to draw conclusions concerning nucleoprotein oligomerization and nucleocapsid condensation of mononegaviruses. Further examples of recent subnanometer-resolution structures include the COPI coat budded in vitro from giant unilamellar vesicles using purified coat protein components (COPI proteins mediate trafficking within the Golgi compartment) (113) and an endoplasmic reticulum translocon-associated ribosome protein complex, observed in rough microsomal membranes or purified in the detergent digitonin (114).

While most of the examples discussed above employed in vitro reconstituted specimen, recent structures from within whole cells offer the prospect of visualizing biological molecules in their native environment in unprecedented detail. Bykov et al. (115) applied focused ion beam milling, cryo-ET, and subtomogram averaging to determine the native structure of the COPI coat protein within the Golgi stacks of *Chlamydomonas reinhardtii*. The native COPI structure resembled that of the in vitro–generated model (113), but additionally uncovered bound cargo. Notably, the unicellular green alga *C. reinhardtii* is a genetically tractable model organism, with reproducible Golgi architecture that allows comparative analysis across multiple cells (115). Vitrified *Chlamydomonas* cells have also been used to visualize the algal translocon-associated protein complex as an integral component of the translocon, assisting the Sec61 protein–conducting channel in transport across or insertion into the endoplasmic reticulum of proteins (116). In addition, two classes of proteasomes tethered to two specific nuclear core complex locations were observed through a combination of subtomogram averaging and nanometer-precision localization (117). Lastly, 3D snapshots into HeLa cells provided insight into the native structure and organization of the cytoplasmic translation machinery, the nuclear core complex, and lamina (118).

5. FUTURE PERSPECTIVE

Given the rapid technological advances in automated high-resolution data collection, processing, and 3D reconstruction, it is reasonable to expect that cryo-EM methods will be suitable for structure determination of ever smaller and asymmetric macromolecules. The methodology is already being tested for screening of binding of drug targets (10, 119, 120), an approach that has historically been reserved for X-ray crystallography and, to a lesser extent, for NMR. Moreover, cryo-EM will likely find its utility in studying large, transient, multisubunit and multicomponent systems that are vital for regulation of cellular processes. Preparation, optimization, and stabilization of a sample will be a major aspect of the next wave of advances in cryo-EM and will drive further advances in structural biology. We can also anticipate substantial improvements in the use and application of cryo-ET to solve important problems in cell biology. More widespread access to rapid data collection, which is becoming increasingly available at regional and national facilities, will likely also be a major catalyst in the adoption of cryo-EM and cryo-ET methods as mainstream tools in biology.

DISCLOSURE STATEMENT

The authors are not aware of any affiliations, memberships, funding, or financial holdings that might be perceived as affecting the objectivity of this review.

ACKNOWLEDGMENTS

The writing of this review was supported by the Intramural Research Program of the National Institutes of Health, National Cancer Institute.

LITERATURE CITED

1. De Zorzi R, Mi W, Liao M, Walz T. 2016. Single-particle electron microscopy in the study of membrane protein structure. *Microscopy* 65:81–96
2. Fernandez-Leiro R, Scheres SHW. 2017. A pipeline approach to single-particle processing in RELION. *Acta Crystallogr. D* 73:496–502
3. Hutchings J, Zanetti G. 2018. Fine details in complex environments: the power of cryo-electron tomography. *Biochem. Soc. Trans.* 46:807–16
4. Koning RI, Koster AJ, Sharp TH. 2018. Advances in cryo-electron tomography for biology and medicine. *Ann. Anat.* 217:82–96
5. Renaud JP, Chari A, Ciferri C, Liu WT, Remigy HW, et al. 2018. Cryo-EM in drug discovery: achievements, limitations and prospects. *Nat. Rev. Drug Discov.* 17:471–92

6. Cheng Y. 2018. Single-particle cryo-EM—how did it get here and where will it go? *Science* 361:876–80
7. Bai XC, Yan C, Yang G, Lu P, Ma D, et al. 2015. An atomic structure of human γ-secretase. *Nature* 525:212–17
8. Dashti A, Schwander P, Langlois R, Fung R, Li W, et al. 2014. Trajectories of the ribosome as a Brownian nanomachine. *PNAS* 111:17492–97
9. Gao Y, Cao E, Julius D, Cheng Y. 2016. TRPV1 structures in nanodiscs reveal mechanisms of ligand and lipid action. *Nature* 534:347–51
10. Subramaniam S, Earl LA, Falconieri V, Milne JL, Egelman EH. 2016. Resolution advances in cryo-EM enable application to drug discovery. *Curr. Opin. Struct. Biol.* 41:194–202
11. Zhou A, Rohou A, Schep DG, Bason JV, Montgomery MG, et al. 2015. Structure and conformational states of the bovine mitochondrial ATP synthase by cryo-EM. *eLife* 4:e10180
12. Lee JH, Ozorowski G, Ward AB. 2016. Cryo-EM structure of a native, fully glycosylated, cleaved HIV-1 envelope trimer. *Science* 351:1043–48
13. Taylor NMI, Manolaridis I, Jackson SM, Kowal J, Stahlberg H, Locher KP. 2017. Structure of the human multidrug transporter ABCG2. *Nature* 546:504–9
14. Bottcher B, Kiselev NA, Stel'Mashchuk VY, Perevozchikova NA, Borisov AV, Crowther RA. 1997. Three-dimensional structure of infectious bursal disease virus determined by electron cryomicroscopy. *J. Virol.* 71:325–30
15. Conway JF, Cheng N, Zlotnick A, Wingfield PT, Stahl SJ, Steven AC. 1997. Visualization of a 4-helix bundle in the hepatitis B virus capsid by cryo-electron microscopy. *Nature* 386:91–94
16. Brown A, Shao S. 2018. Ribosomes and cryo-EM: a duet. *Curr. Opin. Struct. Biol.* 52:1–7
17. Amunts A, Brown A, Bai XC, Llacer JL, Hussain T, et al. 2014. Structure of the yeast mitochondrial large ribosomal subunit. *Science* 343:1485–89
18. Bartesaghi A, Aguerrebere C, Falconieri V, Banerjee S, Earl LA, et al. 2018. Atomic resolution cryo-EM structure of β-galactosidase. *Structure* 26:848–56
19. Tan YZ, Aiyer S, Mietzsch M, Hull JA, McKenna R, et al. 2018. Sub-2 Å Ewald curvature corrected structure of an AAV2 capsid variant. *Nat. Commun.* 9:3628
20. Khoshouei M, Radjainia M, Baumeister W, Danev R. 2017. Cryo-EM structure of haemoglobin at 3.2 Å determined with the Volta Phase Plate. *Nat. Commun.* 8:16099
21. Merk A, Bartesaghi A, Banerjee S, Falconieri V, Rao P, et al. 2016. Breaking cryo-EM resolution barriers to facilitate drug discovery. *Cell* 165:1698–707
22. Banerjee S, Bartesaghi A, Merk A, Rao P, Bulfer SL, et al. 2016. 2.3 Å resolution cryo-EM structure of human p97 and mechanism of allosteric inhibition. *Science* 351:871–75
23. Frank J. 2016. Generalized single-particle cryo-EM—a historical perspective. *Microscopy* 65:3–8
24. Duan J, Li Z, Li J, Hulse RE, Santa-Cruz A, et al. 2018. Structure of the mammalian TRPM7, a magnesium channel required during embryonic development. *PNAS* 115:E8201–10
25. Hahn A, Vonck J, Mills DJ, Meier T, Kuhlbrandt W. 2018. Structure, mechanism, and regulation of the chloroplast ATP synthase. *Science* 360:eaat4318
26. Hulse RE, Li Z, Huang RK, Zhang J, Clapham DE. 2018. Cryo-EM structure of the polycystin 2-l1 ion channel. *eLife* 7:e36931
27. Jackson SM, Manolaridis I, Kowal J, Zechner M, Taylor NMI, et al. 2018. Structural basis of small-molecule inhibition of human multidrug transporter ABCG2. *Nat. Struct. Mol. Biol.* 25:333–40
28. Parmar M, Rawson S, Scarff CA, Goldman A, Dafforn TR, et al. 2018. Using a SMALP platform to determine a sub-nm single particle cryo-EM membrane protein structure. *Biochim. Biophys. Acta* 1860:378–83
29. Qi X, Schmiege P, Coutavas E, Wang J, Li X. 2018. Structures of human Patched and its complex with native palmitoylated sonic hedgehog. *Nature* 560:128–32
30. Rheinberger J, Gao X, Schmidpeter PA, Nimigean CM. 2018. Ligand discrimination and gating in cyclic nucleotide–gated ion channels from apo and partial agonist-bound cryo-EM structures. *eLife* 7:e39775
31. Yoo J, Wu M, Yin Y, Herzik MA Jr., Lander GC, Lee SY. 2018. Cryo-EM structure of a mitochondrial calcium uniporter. *Science* 361:506–11
32. Earl LA, Falconieri V, Milne JL, Subramaniam S. 2017. Cryo-EM: beyond the microscope. *Curr. Opin. Struct. Biol.* 46:71–88

33. Fernandez-Leiro R, Scheres SH. 2016. Unravelling biological macromolecules with cryo-electron microscopy. *Nature* 537:339–46
34. Elmlund D, Le SN, Elmlund H. 2017. High-resolution cryo-EM: the nuts and bolts. *Curr. Opin. Struct. Biol.* 46:1–6
35. Scheres SH. 2016. Processing of structurally heterogeneous cryo-EM data in RELION. *Methods Enzymol.* 579:125–57
36. Frank J. 2017. Time-resolved cryo-electron microscopy: recent progress. *J. Struct. Biol.* 200:303–6
37. Cabra V, Samso M. 2015. Do's and don'ts of cryo-electron microscopy: a primer on sample preparation and high quality data collection for macromolecular 3D reconstruction. *J. Vis. Exp.* 95:52311
38. Chari A, Haselbach D, Kirves JM, Ohmer J, Paknia E, et al. 2015. ProteoPlex: stability optimization of macromolecular complexes by sparse-matrix screening of chemical space. *Nat. Methods* 12:859–65
39. Kastner B, Fischer N, Golas MM, Sander B, Dube P, et al. 2008. GraFix: sample preparation for single-particle electron cryomicroscopy. *Nat. Methods* 5:53–55
40. Thonghin N, Kargas V, Clews J, Ford RC. 2018. Cryo-electron microscopy of membrane proteins. *Methods* 147:176–86
41. Gewering T, Januliene D, Ries AB, Moeller A. 2018. Know your detergents: a case study on detergent background in negative stain electron microscopy. *J. Struct. Biol.* 203:242–46
42. Hauer F, Gerle C, Fischer N, Oshima A, Shinzawa-Itoh K, et al. 2015. GraDeR: membrane protein complex preparation for single-particle cryo-EM. *Structure* 23:1769–75
43. Tribet C, Audebert R, Popot JL. 1996. Amphipols: polymers that keep membrane proteins soluble in aqueous solutions. *PNAS* 93:15047–50
44. Popot JL. 2010. Amphipols, nanodiscs, and fluorinated surfactants: three nonconventional approaches to studying membrane proteins in aqueous solutions. *Annu. Rev. Biochem.* 79:737–75
45. Ritchie TK, Grinkova YV, Bayburt TH, Denisov IG, Zolnerciks JK, et al. 2009. Reconstitution of membrane proteins in phospholipid bilayer nanodiscs. *Methods Enzymol.* 464:211–31
46. Carlson ML, Young JW, Zhao Z, Fabre L, Jun D, et al. 2018. The Peptidisc, a simple method for stabilizing membrane proteins in detergent-free solution. *eLife* 7:e34085
47. Tao H, Lee SC, Moeller A, Roy RS, Siu FY, et al. 2013. Engineered nanostructured β-sheet peptides protect membrane proteins. *Nat. Methods* 10:759–61
48. Postis V, Rawson S, Mitchell JK, Lee SC, Parslow RA, et al. 2015. The use of SMALPs as a novel membrane protein scaffold for structure study by negative stain electron microscopy. *Biochim. Biophys. Acta* 1848:496–501
49. Dubochet J, Adrian M, Chang JJ, Homo JC, Lepault J, et al. 1988. Cryo-electron microscopy of vitrified specimens. *Q. Rev. Biophys.* 21:129–228
50. Dobro MJ, Melanson LA, Jensen GJ, McDowall AW. 2010. Plunge freezing for electron cryomicroscopy. *Methods Enzymol.* 481:63–82
51. D'Imprima E, Floris D, Joppe M, Sanchez R, Grininger M, Kuhlbrandt W. 2018. The deadly touch: protein denaturation at the water–air interface and how to prevent it. bioRxiv 400432. **https://doi.org/10.1101/400432**
52. Pantelic RS, Suk JW, Magnuson CW, Meyer JC, Wachsmuth P, et al. 2011. Graphene: Substrate preparation and introduction. *J. Struct. Biol.* 174:234–38
53. Pantelic RS, Fu W, Schoenenberger C, Henning Stahlberg H. 2014. Rendering graphene supports hydrophilic with non-covalent aromatic functionalization for transmission electron microscopy. *Appl. Phys. Lett.* 104:134103
54. Gatsogiannis C, Merino F, Prumbaum D, Roderer D, Leidreiter F, et al. 2016. Membrane insertion of a Tc toxin in near-atomic detail. *Nat. Struct. Mol. Biol.* 23:884–90
55. Zhang Z, Chen J. 2016. Atomic structure of the cystic fibrosis transmembrane conductance regulator. *Cell* 167:1586–97
56. Dandey VP, Wei H, Zhang Z, Tan YZ, Acharya P, et al. 2018. Spotiton: new features and applications. *J. Struct. Biol.* 202:161–69
57. Glaeser RM, Han BG, Csencsits R, Killilea A, Pulk A, Cate JH. 2016. Factors that influence the formation and stability of thin, cryo-EM specimens. *Biophys. J.* 110:749–55

58. Danev R, Buijsse B, Khoshouei M, Plitzko JM, Baumeister W. 2014. Volta potential phase plate for in-focus phase contrast transmission electron microscopy. *PNAS* 111:15635–40
59. McMullan G, Faruqi AR, Henderson R. 2016. Direct electron detectors. *Methods Enzymol.* 579:1–17
60. Mastronarde DN. 2005. Automated electron microscope tomography using robust prediction of specimen movements. *J. Struct. Biol.* 152:36–51
61. Suloway C, Pulokas J, Fellmann D, Cheng A, Guerra F, et al. 2005. Automated molecular microscopy: the new Leginon system. *J. Struct. Biol.* 151:41–60
62. Grant T, Rohou A, Grigorieff N. 2018. cisTEM, user-friendly software for single-particle image processing. *eLife* 7:e35383
63. Ludtke SJ. 2016. Single-particle refinement and variability analysis in EMAN2.1. *Methods Enzymol.* 579:159–89
64. Punjani A, Rubinstein JL, Fleet DJ, Brubaker MA. 2017. cryoSPARC: algorithms for rapid unsupervised cryo-EM structure determination. *Nat. Methods* 14:290–96
65. Yu L, Franken E, Voigt A, Grollios F, Tiemeijer P, Reyntjens S. 2018. On-the-fly image quality evaluation for single-particle analysis cryo-electron microscopy. *Microsc. Microanal.* 23(Suppl. 1):834
66. Weis WI, Kobilka BK. 2018. The molecular basis of G protein–coupled receptor activation. *Annu. Rev. Biochem.* 87:897–919
67. Scheerer P, Park JH, Hildebrand PW, Kim YJ, Krauss N, et al. 2008. Crystal structure of opsin in its G-protein-interacting conformation. *Nature* 455:497–502
68. Rasmussen SG, DeVree BT, Zou Y, Kruse AC, Chung KY, et al. 2011. Crystal structure of the β_2 adrenergic receptor–Gs protein complex. *Nature* 477:549–55
69. Chae PS, Rasmussen SG, Rana RR, Gotfryd K, Chandra R, et al. 2010. Maltose–neopentyl glycol (MNG) amphiphiles for solubilization, stabilization and crystallization of membrane proteins. *Nat. Methods* 7:1003–8
70. Landau EM, Rosenbusch JP. 1996. Lipidic cubic phases: a novel concept for the crystallization of membrane proteins. *PNAS* 93:14532–35
71. Carpenter B, Nehme R, Warne T, Leslie AG, Tate CG. 2016. Structure of the adenosine A_{2a} receptor bound to an engineered G protein. *Nature* 536:104–7
72. Carpenter B, Tate CG. 2016. Engineering a minimal G protein to facilitate crystallisation of G protein–coupled receptors in their active conformation. *Protein Eng. Des. Sel.* 29:583–94
73. Liang YL, Khoshouei M, Radjainia M, Zhang Y, Glukhova A, et al. 2017. Phase-plate cryo-EM structure of a class B GPCR–G-protein complex. *Nature* 546:118–23
74. Liang YL, Khoshouei M, Glukhova A, Furness SGB, Zhao P, et al. 2018. Phase-plate cryo-EM structure of a biased agonist-bound human GLP-1 receptor–Gs complex. *Nature* 555:121–25
75. Zhang Y, Sun B, Feng D, Hu H, Chu M, et al. 2017. Cryo-EM structure of the activated GLP-1 receptor in complex with a G protein. *Nature* 546:248–53
76. Garcia-Nafria J, Lee Y, Bai X, Carpenter B, Tate CG. 2018. Cryo-EM structure of the adenosine A_{2A} receptor coupled to an engineered heterotrimeric G protein. *eLife* 7:e35946
77. Koehl A, Hu H, Maeda S, Zhang Y, Qu Q, et al. 2018. Structure of the micro-opioid receptor–Gi protein complex. *Nature* 558:547–52
78. Draper-Joyce CJ, Khoshouei M, Thal DM, Liang YL, Nguyen ATN, et al. 2018. Structure of the adenosine-bound human adenosine A_1 receptor–Gi complex. *Nature* 558:559–63
79. Kang Y, Kuybeda O, de Waal PW, Mukherjee S, Van Eps N, et al. 2018. Cryo-EM structure of human rhodopsin bound to an inhibitory G protein. *Nature* 558:553–58
80. Garcia-Nafria J, Nehme R, Edwards PC, Tate CG. 2018. Cryo-EM structure of the serotonin 5-HT_{1B} receptor coupled to heterotrimeric Go. *Nature* 558:620–23
81. Liang Y-L, Khoshouei M, Deganutti G, Glukhova A, Koole C, et al. 2018. Cryo-EM structure of the active, Gs protein complexed, human CGRP receptor. *Nature* 561:492–97
82. Brody E, Abelson J. 1985. The "spliceosome": yeast pre-messenger RNA associates with a 40S complex in a splicing-dependent reaction. *Science* 228:963–67
83. Kondo Y, Oubridge C, van Roon AM, Nagai K. 2015. Crystal structure of human U1 snRNP, a small nuclear ribonucleoprotein particle, reveals the mechanism of 5′ splice site recognition. *eLife* 4:e04986

84. Galej WP, Oubridge C, Newman AJ, Nagai K. 2013. Crystal structure of Prp8 reveals active site cavity of the spliceosome. *Nature* 493:638–43
85. Ramakrishnan V. 2002. Ribosome structure and the mechanism of translation. *Cell* 108:557–72
86. Will CL, Lührmann R. 2011. Spliceosome structure and function. *Cold Spring Harb. Perspect. Biol.* 3:a003707
87. Galej WP, Nguyen TH, Newman AJ, Nagai K. 2014. Structural studies of the spliceosome: zooming into the heart of the machine. *Curr. Opin. Struct. Biol.* 25:57–66
88. Yan C, Wan R, Bai R, Huang G, Shi Y. 2017. Structure of a yeast step II catalytically activated spliceosome. *Science* 355:149–55
89. Bertram K, Agafonov DE, Dybkov O, Haselbach D, Leelaram MN, et al. 2017. Cryo-EM structure of a pre-catalytic human spliceosome primed for activation. *Cell* 170:701–13
90. Bertram K, Agafonov DE, Liu WT, Dybkov O, Will CL, et al. 2017. Cryo-EM structure of a human spliceosome activated for step 2 of splicing. *Nature* 542:318–23
91. Bessonov S, Anokhina M, Krasauskas A, Golas MM, Sander B, et al. 2010. Characterization of purified human Bact spliceosomal complexes reveals compositional and morphological changes during spliceosome activation and first step catalysis. *RNA* 16:2384–403
92. Spillantini MG, Schmidt ML, Lee VM, Trojanowski JQ, Jakes R, Goedert M. 1997. α-Synuclein in Lewy bodies. *Nature* 388:839–40
93. Glenner GG, Wong CW, Quaranta V, Eanes ED. 1984. The amyloid deposits in Alzheimer's disease: their nature and pathogenesis. *Appl. Pathol.* 2:357–69
94. Masters CL, Simms G, Weinman NA, Multhaup G, McDonald BL, Beyreuther K. 1985. Amyloid plaque core protein in Alzheimer disease and Down syndrome. *PNAS* 82:4245–49
95. Auer S. 2015. Nucleation of polymorphic amyloid fibrils. *Biophys. J.* 108:1176–86
96. Fandrich M, Nystrom S, Nilsson KPR, Bockmann A, LeVine H 3rd, Hammarstrom P. 2018. Amyloid fibril polymorphism: a challenge for molecular imaging and therapy. *J. Intern. Med.* 283:218–37
97. Meier BH, Riek R, Bockmann A. 2017. Emerging structural understanding of amyloid fibrils by solid-state NMR. *Trends Biochem. Sci.* 42:777–87
98. Close W, Neumann M, Schmidt A, Hora M, Annamalai K, et al. 2018. Physical basis of amyloid fibril polymorphism. *Nat. Commun.* 9:699
99. Fitzpatrick AWP, Falcon B, He S, Murzin AG, Murshudov G, et al. 2017. Cryo-EM structures of tau filaments from Alzheimer's disease. *Nature* 547:185–90
100. Falcon B, Zhang W, Murzin AG, Murshudov G, Garringer HJ, et al. 2018. Structures of filaments from Pick's disease reveal a novel tau protein fold. *Nature* 561:137–40
101. Guerrero-Ferreira R, Taylor NM, Mona D, Ringler P, Lauer ME, et al. 2018. Cryo-EM structure of α-synuclein fibrils. *eLife* 7:e36402
102. Liu J, Bartesaghi A, Borgnia MJ, Sapiro G, Subramaniam S. 2008. Molecular architecture of native HIV-1 gp120 trimers. *Nature* 455:109–13
103. Wan W, Briggs JA. 2016. Cryo-electron tomography and subtomogram averaging. *Methods Enzymol.* 579:329–67
104. Bartesaghi A, Sprechmann P, Liu J, Randall G, Sapiro G, Subramaniam S. 2008. Classification and 3D averaging with missing wedge correction in biological electron tomography. *J. Struct. Biol.* 162:436–50
105. Hartnell LM, Earl LA, Bliss D, Moran A, Subramaniam S. 2016. Imaging cellular architecture with 3D SEM. In *Encyclopedia of Cell Biology*, ed. RA Bradshaw, PD Stahl, pp. 44–50. Waltham, MA: Academic
106. Hayles MF, de Winter DA, Schneijdenberg CT, Meeldijk JD, Luecken U, et al. 2010. The making of frozen-hydrated, vitreous lamellas from cells for cryo-electron microscopy. *J. Struct. Biol.* 172:180–90
107. Oikonomou CM, Jensen GJ. 2017. Cellular electron cryotomography: toward structural biology in situ. *Annu. Rev. Biochem.* 86:873–96
108. Bharat TAM, Kureisaite-Ciziene D, Hardy GG, Yu EW, Devant JM, et al. 2017. Structure of the hexagonal surface layer on *Caulobacter crescentus* cells. *Nat. Microbiol.* 2:17059

109. Schur FK, Obr M, Hagen WJ, Wan W, Jakobi AJ, et al. 2016. An atomic model of HIV-1 capsid-SP1 reveals structures regulating assembly and maturation. *Science* 353:506–8
110. Wan W, Kolesnikova L, Clarke M, Koehler A, Noda T, et al. 2017. Structure and assembly of the Ebola virus nucleocapsid. *Nature* 551:394–97
111. Turonova B, Schur FKM, Wan W, Briggs JAG. 2017. Efficient 3D-CTF correction for cryo-electron tomography using NovaCTF improves subtomogram averaging resolution to 3.4 Å. *J. Struct. Biol.* 199:187–95
112. Wagner JM, Zadrozny KK, Chrustowicz J, Purdy MD, Yeager M, et al. 2016. Crystal structure of an HIV assembly and maturation switch. *eLife* 5:e17063
113. Dodonova SO, Aderhold P, Kopp J, Ganeva I, Rohling S, et al. 2017. 9 Å structure of the COPI coat reveals that the Arf1 GTPase occupies two contrasting molecular environments. *eLife* 6:e26691
114. Braunger K, Pfeffer S, Shrimal S, Gilmore R, Berninghausen O, et al. 2018. Structural basis for coupling protein transport and *N*-glycosylation at the mammalian endoplasmic reticulum. *Science* 360:215–19
115. Bykov YS, Schaffer M, Dodonova SO, Albert S, Plitzko JM, et al. 2017. The structure of the COPI coat determined within the cell. *eLife* 6:e32493
116. Pfeffer S, Dudek J, Schaffer M, Ng BG, Albert S, et al. 2017. Dissecting the molecular organization of the translocon-associated protein complex. *Nat. Commun.* 8:14516
117. Albert S, Schaffer M, Beck F, Mosalaganti S, Asano S, et al. 2017. Proteasomes tether to two distinct sites at the nuclear pore complex. *PNAS* 114:13726–31
118. Mahamid J, Pfeffer S, Schaffer M, Villa E, Danev R, et al. 2016. Visualizing the molecular sociology at the HeLa cell nuclear periphery. *Science* 351:969–72
119. Merk A, Bartesaghi A, Banerjee S, Falconieri V, Rao P, et al. 2016. Breaking cryo-EM resolution barriers to facilitate drug discovery. *Cell* 165:1698–707
120. Scapin G, Potter CS, Carragher B. 2018. Cryo-EM for small molecules discovery, design, understanding, and application. *Cell Chem. Biol.* 25:1318–25
121. Agafonov DE, Kastner B, Dybkov O, Hofele RV, Liu WT, et al. 2016. Molecular architecture of the human U4/U6.U5 tri-snRNP. *Science* 351:1416–20
122. Rauhut R, Fabrizio P, Dybkov O, Hartmuth K, Pena V, et al. 2016. Molecular architecture of the *Saccharomyces cerevisiae* activated spliceosome. *Science* 353:1399–405
123. Wan R, Yan C, Bai R, Huang G, Shi Y. 2016. Structure of a yeast catalytic step I spliceosome at 3.4 Å resolution. *Science* 353:895–904
124. Zhang X, Yan C, Hang J, Finci LI, Lei J, Shi Y. 2017. An atomic structure of the human spliceosome. *Cell* 169:918–29
125. Yan C, Hang J, Wan R, Huang M, Wong CC, Shi Y. 2015. Structure of a yeast spliceosome at 3.6-angstrom resolution. *Science* 349:1182–91
126. Shen H, Li Z, Jiang Y, Pan X, Wu J, et al. 2018. Structural basis for the modulation of voltage-gated sodium channels by animal toxins. *Science* 362:eaau2596
127. Zhang Z, Toth B, Szollosi A, Chen J, Csanady L. 2018. Structure of a TRPM2 channel in complex with Ca^{2+} explains unique gating regulation. *eLife* 7:e36409
128. Duan J, Li Z, Li J, Santa-Cruz A, Sanchez-Martinez S, et al. 2018. Structure of full-length human TRPM4. *PNAS* 115:2377–82
129. Butterwick JA, Del Marmol J, Kim KH, Kahlson MA, Rogow JA, et al. 2018. Cryo-EM structure of the insect olfactory receptor Orco. *Nature* 560:447–52
130. She J, Guo J, Chen Q, Zeng W, Jiang Y, Bai XC. 2018. Structural insights into the voltage and phospholipid activation of the mammalian TPC1 channel. *Nature* 556:130–34
131. Baradaran R, Wang C, Siliciano AF, Long SB. 2018. Cryo-EM structures of fungal and metazoan mitochondrial calcium uniporters. *Nature* 559:580–84
132. Nguyen NX, Armache JP, Lee C, Yang Y, Zeng W, et al. 2018. Cryo-EM structure of a fungal mitochondrial calcium uniporter. *Nature* 559:570–74
133. Fan C, Choi W, Sun W, Du J, Lu W. 2018. Structure of the human lipid-gated cation channel TRPC3. *eLife* 7:e36852

134. Duan J, Li J, Zeng B, Chen GL, Peng X, et al. 2018. Structure of the mouse TRPC4 ion channel. *Nat. Commun.* 9:3102
135. Vinayagam D, Mager T, Apelbaum A, Bothe A, Merino F, et al. 2018. Electron cryo-microscopy structure of the canonical TRPC4 ion channel. *eLife* 7:e36615
136. Paknejad N, Hite RK. 2018. Structural basis for the regulation of inositol trisphosphate receptors by Ca^{2+} and IP3. *Nat. Struct. Mol. Biol.* 25:660–68
137. Park E, MacKinnon R. 2018. Structure of the CLC-1 chloride channel from *Homo sapiens*. *eLife* 7:e36629
138. Lee CH, MacKinnon R. 2018. Activation mechanism of a human SK-calmodulin channel complex elucidated by cryo-EM structures. *Science* 360:508–13
139. Deneka D, Sawicka M, Lam AKM, Paulino C, Dutzler R. 2018. Structure of a volume-regulated anion channel of the LRRC8 family. *Nature* 558:254–59
140. Yoder N, Yoshioka C, Gouaux E. 2018. Gating mechanisms of acid-sensing ion channels. *Nature* 555:397–401
141. Qian P, Siebert CA, Wang P, Canniffe DP, Hunter CN. 2018. Cryo-EM structure of the *Blastochloris viridis* LH1–RC complex at 2.9 Å. *Nature* 556:203–8
142. Pan X, Ma J, Su X, Cao P, Chang W, et al. 2018. Structure of the maize photosystem I supercomplex with light-harvesting complexes I and II. *Science* 360:1109–13
143. Pi X, Tian L, Dai HE, Qin X, Cheng L, et al. 2018. Unique organization of photosystem I light-harvesting supercomplex revealed by cryo-EM from a red alga. *PNAS* 115:4423–28
144. Roh SH, Stam NJ, Hryc CF, Couoh-Cardel S, Pintilie G, et al. 2018. The 3.5-Å cryoEM structure of nanodisc-reconstituted yeast vacuolar ATPase V_0 proton channel. *Mol. Cell* 69:993–1004
145. Srivastava AP, Luo M, Zhou W, Symersky J, Bai D, et al. 2018. High-resolution cryo-EM analysis of the yeast ATP synthase in a lipid membrane. *Science* 360:eaas9699
146. Agip AA, Blaza JN, Bridges HR, Viscomi C, Rawson S, et al. 2018. Cryo-EM structures of complex I from mouse heart mitochondria in two biochemically defined states. *Nat. Struct. Mol. Biol.* 25:548–56
147. Yu H, Wu CH, Schut GJ, Haja DK, Zhao G, et al. 2018. Structure of an ancient respiratory system. *Cell* 173:1636–49
148. Sun C, Benlekbir S, Venkatakrishnan P, Wang Y, Hong S, et al. 2018. Structure of the alternative complex III in a supercomplex with cytochrome oxidase. *Nature* 557:123–26
149. Kim Y, Chen J. 2018. Molecular structure of human P-glycoprotein in the ATP-bound, outward-facing conformation. *Science* 359:915–19
150. Alam A, Kung R, Kowal J, McLeod RA, Tremp N, et al. 2018. Structure of a zosuquidar and UIC2-bound human–mouse chimeric ABCB1. *PNAS* 115:E1973–72
151. Phulera S, Zhu H, Yu J, Claxton DP, Yoder N, et al. 2018. Cryo-EM structure of the benzodiazepine-sensitive $\alpha1\beta1\gamma2S$ tri-heteromeric GABAA receptor in complex with GABA. *eLife* 7:e39383
152. Walsh RM Jr., Roh SH, Gharpure A, Morales-Perez CL, Teng J, Hibbs RE. 2018. Structural principles of distinct assemblies of the human $\alpha4\beta2$ nicotinic receptor. *Nature* 557:261–65
153. Garaeva AA, Oostergetel GT, Gati C, Guskov A, Paulino C, Slotboom DJ. 2018. Cryo-EM structure of the human neutral amino acid transporter ASCT2. *Nat. Struct. Mol. Biol.* 25:515–21
154. Wild R, Kowal J, Eyring J, Ngwa EM, Aebi M, Locher KP. 2018. Structure of the yeast oligosaccharyltransferase complex gives insight into eukaryotic *N*-glycosylation. *Science* 359:545–50
155. Gong X, Qian H, Cao P, Zhao X, Zhou Q, et al. 2018. Structural basis for the recognition of Sonic Hedgehog by human Patched1. *Science* 361:eaas8935
156. Ruan J, Xia S, Liu X, Lieberman J, Wu H. 2018. Cryo-EM structure of the gasdermin A3 membrane pore. *Nature* 557:62–67

Annual Review
of Biomedical
Engineering

Volume 21, 2019

Contents

Errata

An online log of corrections to *Annual Review of Biomedical Engineering* articles may be found at http://www.annualreviews.org/errata/bioeng